SRC-CT Analysis Note for Measurement of J/ψ Near and Below Threshold

J.R. Pybus[1] and L. Ehinger[1]

[1]MIT, Cambridge, MA

December 6, 2023

Abstract

We report on the first measurement of J/ψ photoproduction from nuclei in the photon threshold energy region of $E_\gamma < 10.6$ GeV as well as below the threshold energy $E_\gamma \sim 8.2$ GeV. These data were measured using a tagged photon beam incident on nuclear targets deuterium, helium, and carbon, searching for the semi-inclusive reaction $A(\gamma, e^+e^-p)$ with dilepton mass $M(e^+e^-) \sim m_{J/\psi} = 3.1$ GeV. We examine the cross-section for incoherent J/ψ photoproduction across nuclei and place limits on substantial deviations from plane-wave predictions. In helium and carbon we observe "sub-threshold" production of J/ψ from photons with energies below the proton energy threshold 8.2 GeV, and comment on the implications on nuclear structure.

Contents

1 Introduction

The partonic structure of nuclei has been an outstanding question in nuclear physics since the discovery of the EMC effect [1, 2, 3, 4, 5, 6, 7], which first observed that the structure functions of bound nucleons differ from those of free nucleons. In the decades since this discovery, many high-precision measurements from a large number of nuclei have furthered our knowledge of the modification of quarks in nuclei, but the underlying cause of this effect remains unknown [8, 9, 10, 11]. Studies on the EMC effect, which is dominant in the valence region $0.3 \lesssim x \lesssim 0.7$, have focused on the quark sector, as deep-inelastic scattering is well-suited to measuring quarks in this region. However, there are as yet no similar constraints on the gluon structure of the nucleus in these regions.

With the recent 12 GeV upgrade of the Jefferson Lab CEBAF accelerator, substantial progress has been made in measuring the production of J/ψ from protons in the near-threshold energy region [12, 13, 14]. As protons lack a substantial intrinsic charm content, the production of charmonium is understood to be mediated primarily by the exchange of gluons. These interactions are sensitive to the gluon density of the probed hadrons, with longitudinal momentum fraction $x \approx m_{J/\psi}^2/2m_N E_\gamma$ set by the energy of the incoming photon beam. These studies, which include data measured in experimental Hall D, have provided the first experimental insights into the high-x gluon content of the proton.

Photoproduction of J/ψ from nuclear targets has the potential to give similar understanding of the gluon content of nuclei and bound nucleons. In particular, the "sub-threshold" photoproduction of charmonium using photons with energy below $E_\gamma^{th} \approx 8.2$ GeV has long been sought after as a signature of high-energy gluon configurations in the nucleus [15, 16, 17]. More recently it has been understood that high-energy gluons could result largely from high-momentum nucleons in Short-Range Correlated (SRC) pairs [18]. Sub-threshold production of J/ψ has the potential to be sensitive to a number of exotic effects in nuclei, such as the modification of gluons in SRCs or hidden-color components of the nucleus [19], and is therefore a valuable measurement for our understanding of nuclear structure in extreme conditions.

Few measurements of low-energy J/ψ photoproduction from nuclei have been performed to date [20, 21], and these measurements have been limited, measuring only the inclusive production of J/ψ and having no direct knowledge of the incident photon energy. A dedicated search for sub-threshold production of J/ψ has also been made [17], but was performed at energies far below threshold and observed no events.

In this note, we present the first measurement of J/ψ production from nuclear targets in the near- and sub-threshold region of $7 < E_\gamma < 10.6$ GeV. These events are identified by the detection of semi-inclusive $A(\gamma, e^+e^-p)$, following the leptonic decay $J/\psi \to e^+e^-$. The detection of a knocked-out proton allows both an improved reconstruction of the dilepton mass and an inference of the initial-state nucleon momentum, allowing an examination of the nuclear effects present in the reaction. We observe a small but significant number of J/ψ events from photons with energy $E_\gamma < 8.2$ GeV, marking the first such observation of sub-threshold production of charmonium. We characterize these events and comment on the implications of the measurement.

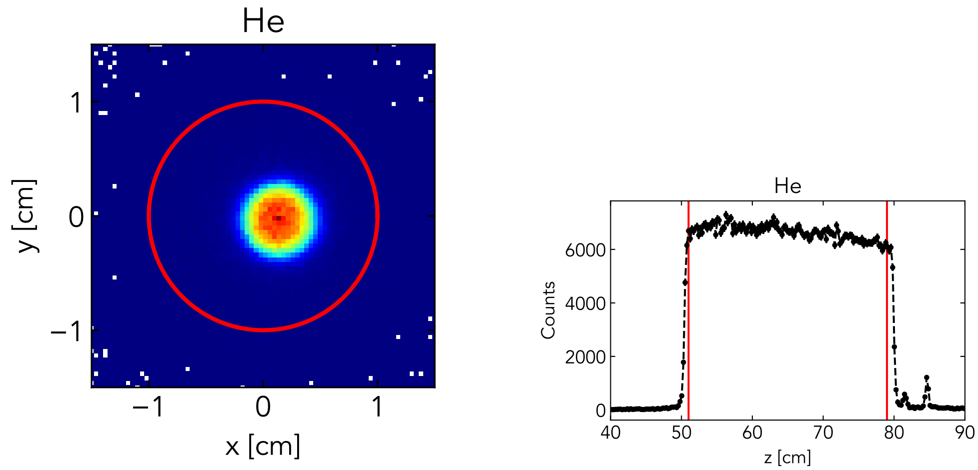

Figure 1: *Left:* Confidence level for the kinematic fit for candidate events from helium. Confidence level was required to be greater than 10^{-3}. *Right:* PID figure-of-merit for proton candidates in helium events. FOM was required to be greater than 10^{-2}.

2 Event Selection

Events measured in the GlueX spectrometer were selected with the purpose of identifying $(\gamma, e^+e^-p)X$ events resulting from the photoproduction of a J/ψ. Data from all nuclei using the `ver01` calibration was skimmed using standard `halld_recon` software and the ReactionFilter plugin (`ver07` skims). The ReactionFilter was used to specify the desired final-state consisting of $e^+e^-p(X)$ and selected all candidate events. While the ReactionFilter is typically used to perform kinematic fitting for exclusive reactions, this measurement is inclusive; as such, the only constraint used was the requirement of a common vertex for all tracks, and no momentum constraints were used. The skim allowed events with up to one additional charged track and two additional showers, and also recorded beam photon hits from the four beam bunches before and after the bunch associated with the RF time.

Results of the reconstruction skim were further processed using the DSelector macro [22]. At this stage further cuts were places on the selected events. No cuts were placed on the PID of the knocked-out proton, as this was found not to improve signal significance following lepton PID. Beam photons were required to have energies $E_\gamma > 7$ GeV, as luminosity at lower energies is more challenging to model and contributes very little to J/ψ production. Charged particles were required to have a momentum $p > 0.4$ GeV, as well as an angle $\theta > 2^\circ$ to avoid the beamline. In order to limit the data to the region of J/ψ production and the surrounding backgrounds, the invariant dilepton mass was restricted to $0.8 < M_{ee} < 3.5$ GeV.

Further cuts were applied to the output of the DSelector. Events with additional tracks or showers in the detector were rejected. The vertex of each event was required to originate within the target, with $51 < z < 79$ cm and $\sqrt{x^2 + y^2} < 1$ cm, as shown in Fig. 1. The energy balance of the reaction with a photon candidate was restricted, requiring the one-nucleon "missing energy" $E_{miss} \equiv E_\gamma + m_N - E_{e^+} - E_{e^-} - E_p$ to be small, $|E_{miss}| < 1$, as shown in Fig. 2. The invariant dilepton mass was further restricted to $M_{ee} > 2$ GeV.

Tagged beam photons were associated with an event if they fell within 2 ns of the RF

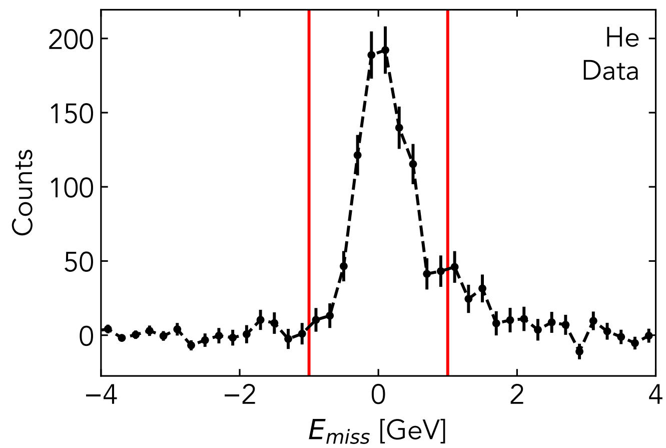

Figure 2: Missing energy distribution for candidate events from helium, including accidental beam photon subtraction. The elastic peak with no missing energy can be seen, as well as a tail extending to nonzero missing energy.

time. To account for the substantial rate of accidental photons in the tagger, off-time photons between 6 and 18 ns from the RF time of the event were taken as a measurement of the photon pileup to be subtracted from the data via event-mixing.

2.1 Lepton PID

Identification of the electron and positron in this reaction is the primary challenge in reducing background from $\pi^+\pi^-p(X)$ production. Previous measurements [23, 24] of J/ψ production in GlueX (performed using hydrogen targets) used two methods to perform electron/pion (e/π) separation by examining the charged particle showers in the calorimeters.

For lepton candidates impacting in the Barrel Calorimeter (BCAL), which covers angles $\theta > 11^\circ$, the inner layer of the the calorimeter was used as a pre-shower detector, and the energy deposition in this layer was required to satisfy $E_{pre}\sin\theta > 30$ MeV, where the $\sin\theta$ factor accounts for the path length of the particle in the layer. Pions deposit much less energy in this region than electrons, allowing for significant rejection of pinon backgrounds. Fig. 3 shows the distribution of this scaled preshower energy for the data compared to the signal simulation. The same cut value was selected in this case as for the previous Hall D analyses, as the BCAL was not different between the experimental setups.

Further electron/pion separation is performed by selecting on p/E, where p is the measured momentum of the charged particle from the kinematic fit and E is the energy deposition of this particle in the calorimeter. Electrons and positrons deposit almost all their energy in the calorimeters, whereas pions deposit only a small fraction; as such, requiring $p/E \sim 1$ significantly reduces the background of the pion. The previous J/ψ analyses in Hall D required $-3\sigma < p/E - \langle p/E\rangle < +2\sigma$ for both lepton candidates, where the resolution σ for the lepton p/E is determined separately for FCAL and BCAL showers.

As this measurement of p differs in resolution from exclusive $\gamma p \to e^+e^-p$ with a full kinematic fit, the values of these resolutions were determined from the candidate leptons in our data. Events with one lepton candidate impacting the FCAL and the other lep-

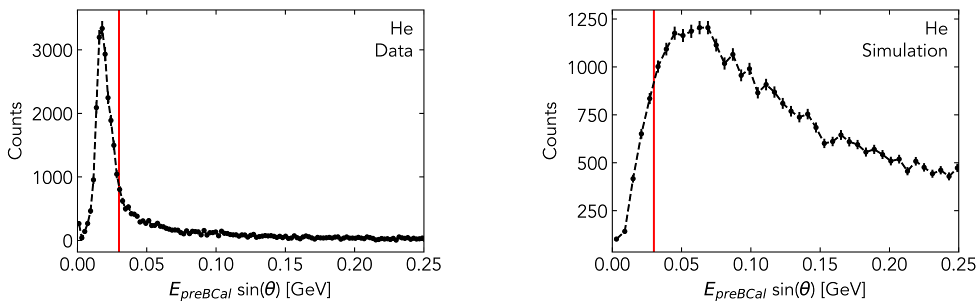

Figure 3: Helium data (left) compared with $(\gamma, J/\psi p)$ simulation (right) for the scaled preshower energy for lepton candidates impacting the BCAL. In data a large fraction of lepton candidates deposit little energy in the preshower layer, while simulated leptons deposit much more energy.

ton impacting the BCAL were used to separately measure the resolution in p/E for each calorimeter, with the resolution assumed to be similar for electrons and positrons. In each axis, a signal slice $-3\sigma < p/E - \langle p/E \rangle < +2\sigma$ was compared with a background slice $+3.5\sigma < p/E - \langle p/E \rangle < +5.5\sigma$ to account for pion contribution under the lepton peak; a slice along the BCAL axis allows one to examine the FCAL p/E, and vice versa. Fig. 4 shows an example of such a slice used to measure the p/E resolution for FCAL candidates, where regions of the BCAL were used to determine signal and background in the FCAL p/E distributions.

Comparison between background and signal slices allows measurement of the resolution on p/E for leptons: the background slice is fit with a fourth order polynomial in order to determine the shape of the pion contribution, and this background model, along with a Gaussian description of the $p/E \sim 1$ peak, are fit to the signal slice, with the normalization of each component allowed to vary. Measurement of the resolution for one calorimeter allows refinement of the signal and background slices for measuring the other calorimeter, and this process was iterated to determine the resolution on p/E separately for the FCAL and the BCAL, found to be 8% and 7%, respectively. These values, particularly the FCAL, are found to deviate somewhat from those observed in the GlueX analysis. This is primarily a result of the worse momentum resolution on charged particles, particularly in the forward region. As this reaction is not exclusive, kinematic fitting does not allow improvement of the momentum resolution for charged particles using the beam photon information, and the longitudinal momentum component is reconstructed more poorly.

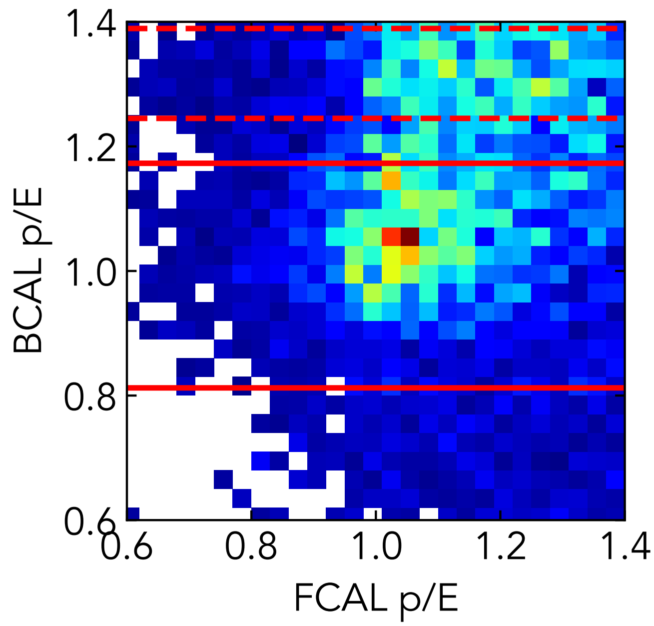

Figure 4: Helium p/E distribution for the two lepton candidates in events with one FCAL (x-axis) and one BCAL (y-axis) candidate. Signal and background regions for measuring the FCAL resolution are indicated with the horizontal red lines; similar vertical slices were used for measuring the BCAL resolution.

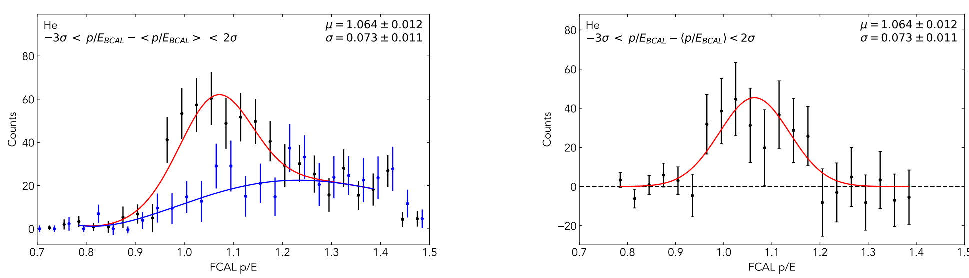

Figure 5: *Left:* Distributions of p/E for helium FCAL lepton candidates, including the signal slice (black) and the background slice (blue) normalized to the same background contribution. The background polynomial fit (blue line) and as well as the Gaussian signal (red line) are shown with the data. *Left:* Difference between signal and background slices, normalized to the fit coefficient for the polynomial background contribution. The Gaussian description of the lepton signal is also shown.

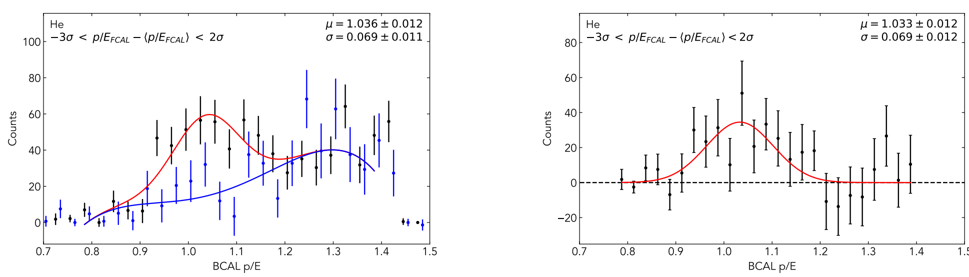

Figure 6: Same as Fig. 6 but for helium BCAL lepton candidates.

3 Observables

The primary means of selecting $J/\psi \to e^+e^-$ decays in data is examining the invariant mass of the dilepton system. This requires reconstructing the 4-momentum of each lepton candidate and taking the square of the sum of these momenta:

$$M^2_{e^+e^-} = (p_{e^+} + p_{e^-})^2 \tag{1}$$

In exclusive $\gamma p \to e^+e^-p$ events, this invariant mass is well-reconstructed, as kinematically fitting the event with the requirement of full 4-momentum conservation leads to well-reconstructed lepton momentum. In non-exclusive $\gamma A \to e^+e^-p(X)$ events, such restrictive kinematic fitting is not possible, and the resulting lepton momenta are more poorly reconstructed, leading to a similarly poor reconstruction for the dilepton mass $M_{e^+e^-}$.

We note that not all components of momentum are reconstructed equally well. In the solenoid magnetic field of GlueX, the transverse component of momentum $\vec{p}^{\perp}$ can be reconstructed with good precision from the curvature of the tracks in the draft chambers. The longitudinal component p^z and the energy E are more poorly reconstructed, requiring a combination of the longitudinal momentum component and the polar angle θ of the track. The use of "light front" variable can help to mitigate these challenges. The energy and longitudinal momentum can be expressed in two linear combinations, denoted the "plus" and "minus" components of momentum:

$$p^{\pm} = E \pm p^z \tag{2}$$

These variables have previously been used in analysis of nucleon knockout data with poor momentum resolution [25]. While the "plus" component of momentum is still poorly reconstructed, the "minus" component, representing the difference between the energy and longitudinal momentum, suffers very little smearing as a result of detector resolution.

$$\frac{\partial p^-}{\partial p_z} = \frac{p_z}{E} - 1 = \mathcal{O}\left(p_\perp^2/p_z^2\right) \tag{3}$$

This effect, combined with the relatively small smearing for the transverse components of momentum in GlueX (a consequence of the solenoid magnet), provides us a combination of momentum variables that may be reliably used to describe the initial nuclear state. We note that for the final-state proton, which is low momentum, the impact of smearing is relatively small in reconstructed variables; for the high-momentum final-state leptons, this smearing is much larger, and thus the plus components of the lepton momentum $p^+_{e^\pm}$ are the most affected.

In the case of the semi-inclusive production from deuterium $\gamma d \to e^+e^-p(n)$, the requirement of a missing neutron provides an additional constraint on the momentum of the final-state particles. We may define the missing mass

$$m^2_{miss} = (p_\gamma + p_d - p_{e^+} - p_{e^-} - p_p)^2\,, \tag{4}$$

where p_γ is the 4-momentum of the beam photon, p_d is the 4-momentum of a deuteron at rest in the lab frame, and p_p is the momentum of the detected proton. In the case of a deuteron target, $m_{miss} = m_N$ is an equality.

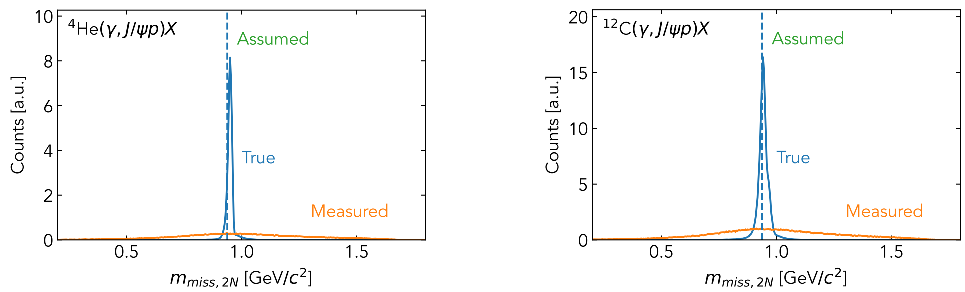

Figure 7: *Left:* Reconstructed (orange) and thrown (blue) values for the two-nucleon missing mass in J/ψ production from helium. The true thrown value can be seen to be very close to the nucleon mass, while the measured value suffers substantial resolution effects. *Right:* Same as left, but for carbon.

The dilepton mass may be expressed in terms of the missing mass, the beam photon energy, and the well-reconstructed "minus" components of the final-state momenta

$$M^2_{e^+e^-} = \left(p^-_{e^+} + p^-_{e^-}\right)\left(2E_\gamma + m_d - p^+_p - \frac{m^2_{miss} + p^2_{tot,\perp}}{m_d - p^-_{tot}}\right) - \left(\vec{p}^{\perp}_{e^+} + \vec{p}^{\perp}_{e^-}\right)^2 \qquad (5)$$

where the "total" momentum $p_{tot} \equiv p_{e^+} + p_{e^-} + p_p$ has been defined for brevity's sake. While this definition does rely on the plus component p^+_p of the proton momentum, it is entirely independent of either lepton plus momentum $p^+_{e^\pm}$, which are the primary source of resolution effects on the dilepton mass. In the case of deuterium, this equation may be used exactly with the insertion $m_{miss} \to m_N$.

In the case of other nuclei, we may still define a "two-nucleon missing mass":

$$m^2_{miss,2N} = \left(p_\gamma + p_{2N} - p_{e^+} - p_{e^-} - p_p\right)^2, \qquad (6)$$

where p_{2N} is the 4-momentum of a nucleon pair at rest in the lab frame. This "missing mass" definition assumes that the struck nucleon in the reaction was recoiled against by a single spectator nucleon, which carried the missing energy and momentum of the reaction. This is an approximation, as in most cases the full nucleus carries the recoil 4-momentum. However, we observe in Fig. 7 that the two-nucleon missing mass can be seen to be very close to the nucleon mass.

As such, the previous relationship between the dilepton mass and the two-nucleon missing mass can still be helpful; by performing the substitution $m_{miss,2N} \to m_N$ we may construct a proxy for the dilepton mass which suffers far less from the impact of detector resolution, allowing isolation of $J/\psi \to e^+e^-$ decays above background.

$$M^2_{e^+e^-} \approx M^2_{e^+e^-,2N} = \left(p^-_{e^+} + p^-_{e^-}\right)\left(2E_\gamma + 2m_N - p^+_p - \frac{m^2_N + p^2_{tot}}{2m_N - p^-_{tot}}\right) - \left(\vec{p}^{\perp}_{e^+} + \vec{p}^{\perp}_{e^-}\right)^2 \qquad (7)$$

Fig. 8 shows the impact of smearing in simulated $\gamma A \to J/\psi p$ events. The reconstructed dilepton mass using the measured lepton momentum can be seen to suffer considerable resolution effects, resulting in a mass resolution of ~ 70 MeV. In contrast, the "2N-proxy" mass is far less impacted by detector smearing, with a mass resolution of 25-30 MeV, a factor of 2.5 better.

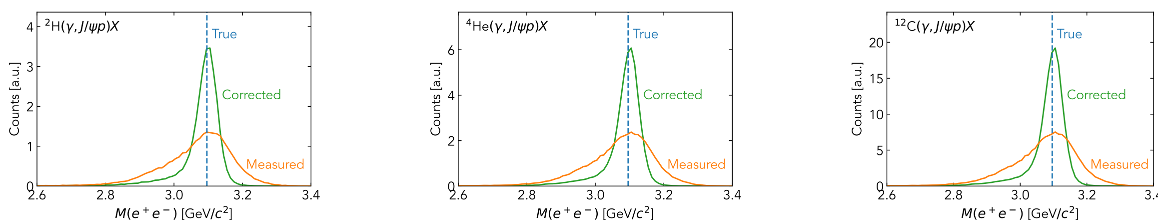

Figure 8: *Left:* Measured dilepton mass (orange), compared with the corrected mass using the 2N-breakup assumption (green) in simulated J/ψ production from deuterium. Also shown is the true J/ψ mass of 3.096 GeV/c^2 (blue). The corrected mass observable shows significantly improved resolution compared with the measured mass. *Center:* Same as left, but for helium. *Right:* Same as left, but for carbon.

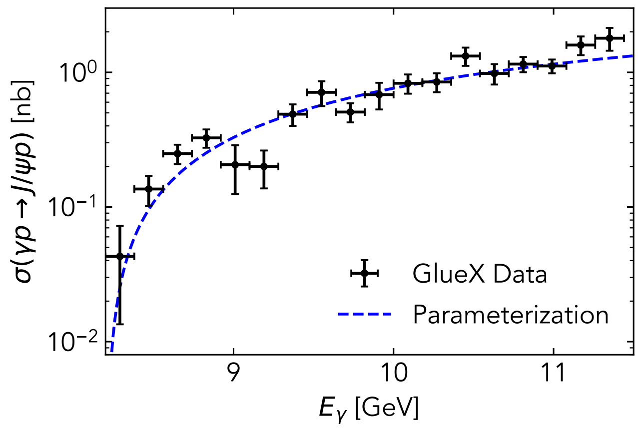

Figure 9: Total $\gamma p \to J/\psi p$ cross section measurements of Ref. [14] (black) compared with analytic parameterization (blue).

4 Monte Carlo

The quasi-elastic channel $(\gamma, J/\psi p)$ was simulated using a factorized cross section model in the Plane-Wave Impulse Approximation (PWIA):

$$\frac{d\sigma(\gamma A \to J/\psi p X)}{dt d^3 p_{miss} dE_{miss}} = v_{\gamma i} \cdot \frac{d\sigma}{dt}(\gamma p \to J/\psi p) \cdot S(p_{miss}, E_{miss}) \tag{8}$$

where $v_{\gamma i} = p_\gamma \cdot p_i / (E_\gamma E_i)$ is the relative velocity between the photon and the struck proton i, and the differential cross section $d\sigma/dt$ for the exclusive process $(\gamma p \to J/\psi p)$ was taken from a fit to GlueX data [14], This fit took the functional form for the total cross section following Refs. [19, 26]

$$\sigma_{tot} = \sigma_0 \cdot (1-\chi)^\beta \tag{9}$$

where

$$\chi = (m_{J/\psi}^2 + 2 m_p m_{J/\psi})/(s_{\gamma p} - m_p^2) \tag{10}$$

and the values $\sigma_0 = 5.9$ nb and $\beta = 1.2$ were found fitting to data, as shown in Fig. 9. The t-dependence of the cross section was assumed to follow a dipole form $F(t) \sim \frac{1}{(1-t/m_s^2)^2}$, using a weighted average $m_s = 1.35 \pm 0.04$ for the dipole parameter following extractions in Ref. [14], assuming weak dependence on $s_{\gamma p}$.

The spectral functions $S(p_{miss}, E_{miss})$ for helium and carbon were taken from Ref. [27] for the mean-field component and the Generalized Contact Formalism [28, 29, 30] for the SRC component, calculated using the phenomenological AV18 interaction [31]. The momentum distribution for deuterium was taken from Ref. [32], again calculated using the AV18 interaction. The produced J/ψ was assumed to conserve the helicity of the incoming photon, with the decay following a $(1 + \cos^2 \theta_{GJ})$ distribution in the Gottfried-Jackson frame. The generated PWIA events were simulated using the GEANT model of the GlueX detector [33], and were reconstructed using standard GlueX reconstruction software in the same manner as measured data.

4.1 Efficiency

The results of Monte Carlo simulation are used to estimate the efficiency for detecting $\gamma A \to J/\psi pX$ events. We use simulations of the three nuclei and compare the yield before and after the application of detector efficiencies, smearing, and selection cuts to determine the fraction of events which pass each level of selection

We note that the GlueX Monte Carlo has been validated against Bethe-Heitler data in previous studies of J/ψ production at GlueX [14]. This study found generally good agreement between data and simulation, but noted a discrepancy in the normalization between simulation and data. The study estimated a 20% uncertainty on the normalization of J/ψ data when using simulated efficiency calculations and multiplied the Monte-Carlo-calculated efficiency by a factor of 0.847 ± 0.019; we therefore assign the same uncertainty on our extracted cross sections and perform the same correction on the calculated efficiencies.

4.2 Proton Transparency

As the final state measured in this reaction includes both the $J/\psi \to e^+e^-$ decay and the knocked-out proton, the effects of nuclear transparency must be considered. For the J/ψ, this effect can be neglected because even in the case of rescattering, the leptonic decay will still be detected and overall yields will be unaffected. For the proton, the transparency factor must be accounted for in determining the cross section.

In the case of deuterium, measurements of $(e, e'p)$ quasi-elastic scattering [34, 35] may be used to determine a data-driven estimate of $90 \pm 1\%$ transparency on protons at $\mathcal{O}(1 \text{ GeV})$ momentum, with little deviation as a function of momentum.

Further details to be expanded on for the calculation of helium and carbon transparency.

5 Normalization

The determination of the absolute cross section for $\gamma A \to J/\psi pX$ is performed by using the measured γA luminosity as well as efficiencies calculated from the Monte Carlo simulations. The cross section may be determined using the formula

$$\sigma(E_\gamma) = \frac{Y(E_\gamma)}{\mathcal{L}(E_\gamma) \times \epsilon(E_\gamma) \times B(J/\psi \to e^+e^-)} \tag{11}$$

where Y is the yield of $J/\psi pX$ events, $\mathcal{L}$ is the luminosity for the nucleus in the energy range of interest, ϵ is the detection and cut efficiency for the e^+e^-p final-state in the kinematics of interest, and $B(J/\psi \to e^+e^-)$ is the branching fraction of J/ψ to e^+e^-.

Appendix A describes the measurement of the tagged beam photon flux f on the target using the Hall D Pair Spectrometer. The calculated luminosity $\mathcal{L}$ requires knowledge also of the target length L and number density N:

$$\mathcal{L} = f \times L \times N \tag{12}$$

We note that the dominant systematic uncertainties on individual flux measurements are related to the acceptance and efficiency of the Pair Spectrometer, and therefore cancel in a ratio.

We also note that the photon flux and luminosity must be defined both in terms of the *tagged* number of photons (that is, the number of beam photons which can be reconstructed using a measured electron) and as a function of the beam photon energy; as such, any values of flux or luminosity represent an integral of some range of measured photon energies. Table 1 shows the measured beam photon flux and luminosity in the energy range $6 < E_\gamma < 10.8$ GeV.

Table 1: Tagged flux and luminosity for each target and for beam photons with energy $6 < E_\gamma < 10.8$ GeV.

Nucleus	Tagged Photon Flux (10^{12})	Tagged Luminosity ($\text{pb}^{-1}\cdot$nucleon)
Deuterium	12.4	35.9
Helium	31.0	66.9
Carbon	51.0	103.5

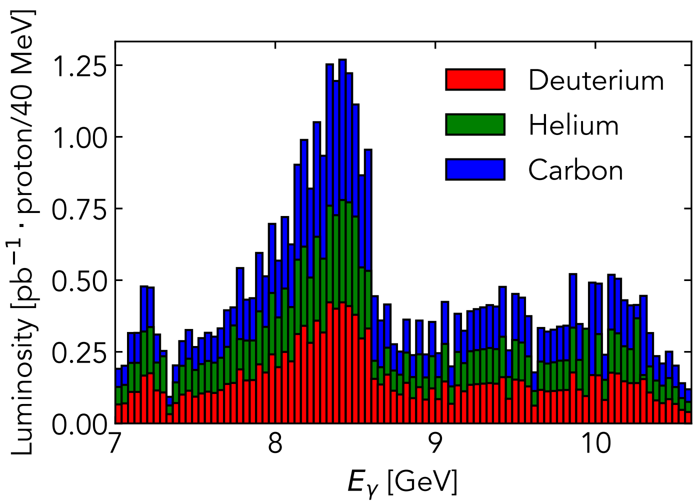

Figure 10: Tagged luminosity for each target in bins of beam photon energy.

6 Systematic Uncertainties

Section to be completed. Point-to-point systematic uncertainties include luminosity, efficiency, yield extraction, and cut dependence. Overall normalization uncertainties include luminosity, efficiency, and nuclear transparency.

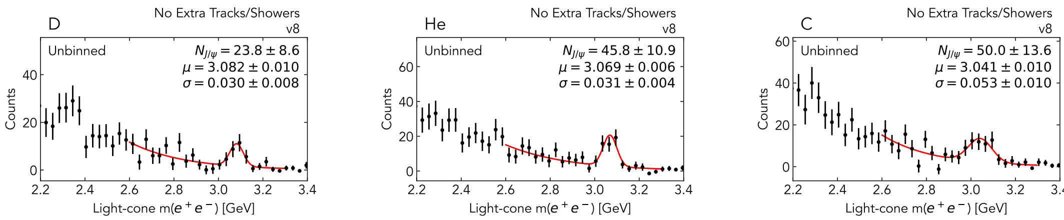

Figure 11: Dilepton invariant mass spectrum in the full photon energy range $7 < E_\gamma < 10.6$ GeV, above the proton energy threshold. The production of J/ψ can be seen by observing peaks near $M(e^+e^-) \sim 3.1$ GeV, with some shifting due to proton rescattering.

Table 2: $J/\psi \to e^+e^-$ yields for each nucleus as a function of beam photon energy.

Nucleus	$7 \div 8.2$ GeV	$8.2 \div 9.5$ GeV	$9.5 \div 10.6$ GeV	$8.2 \div 10.6$ GeV	$7 \div 10.6$ GeV
Deuterium	-	7.7 ± 4.0	16.1 ± 6	21.7 ± 7.8	23.8 ± 8.6
Helium	7.2±4.5	27.7 ± 8.0	15.8 ± 6.4	40.3 ± 10.2	45.8 ± 10.9
Carbon	7.6±3.9	15.1 ± 6.7	31.6 ± 13.2	43.7 ± 14.0	50.0 ± 13.6

7 Results

In Fig. 11 we examine the distribution for the dilepton invariant mass using the previously-described "2N-proxy" variable. For each nucleus we observe statistically significant peaks in the vicinity of the expected J/ψ mass $m_{J/\psi} = 3.096$ GeV. We note that the exact locations and widths of these peaks is subject to some distortion which differs across nuclei. This is believed to be an effect of final-state interactions on the relatively low-momentum outgoing proton. As the proton is used in the reconstruction of the dilepton invariant mass, changes in its outgoing momentum result in distortions of the J/ψ peak. This effect increases with the size of the nucleus, causing the observed trend as a function of A.

In Fig. 12 we examine these dilepton invariant mass spectra as a function of the beam photon energy E_γ. We split the spectra into three bins: the low-energy sub-threshold region $7 < E_\gamma < 8.2$ GeV, the medium-energy region $8.2 < E_\gamma < 9.5$ GeV, and the high-energy region $9.5 < E_\gamma < 10.6$ GeV. For deuterium, the statistical accuracy of the data does not allow a clear examination of the energy-dependence of the cross section. For helium and carbon, however, the dilepton mass spectrum in each energy bin clearly shows a peak from $J/\psi \to e^+e^-$ decay. Notably, this includes the sub-threshold energy region, with photons too low-energy to produce J/ψ from a standing proton.

In Fig. 13 we show the dilepton invariant mass spectrum when combining the data from helium and carbon targets, both of which showed indications of sub-threshold production (unlike deuterium). The combined spectrum shows a more substantial indication of $J/\psi \to e^+e^-$ production, though statistics in the sub-threshold energy region remain highly limited. Nonetheless, this measurement marks the first observation of sub-threshold photoproduction of J/ψ in γA collisions.

From these spectra we extract the yield of $J/\psi \to e^+e^-$ decays in the data as a function of the photon energy E_γ. Table 2 shows the extracted yields for each nucleus in different bins of energy.

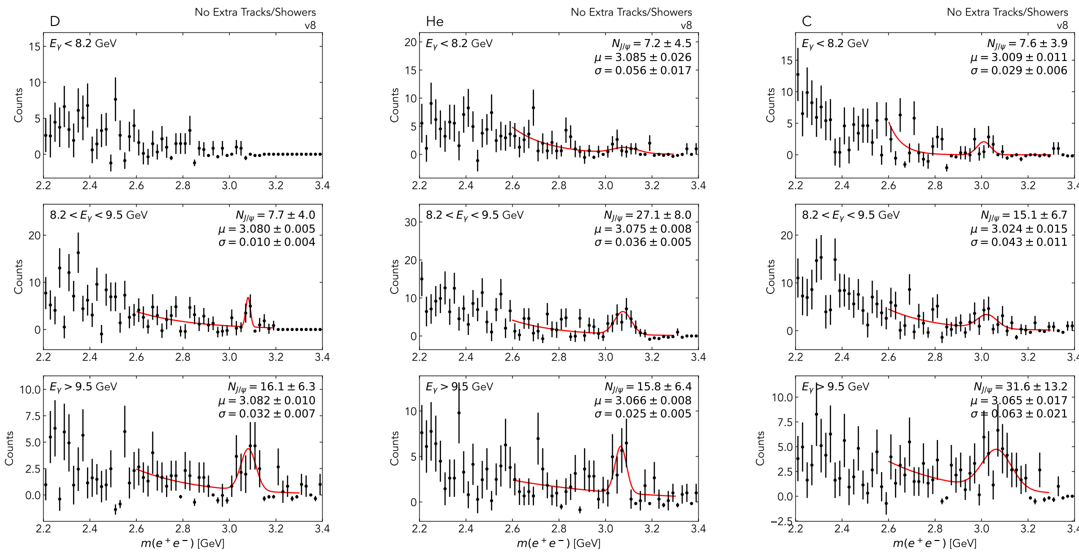

Figure 12: Same as Fig. 11, but split into $7 < E_\gamma < 8.2$ GeV (top), $8.2 < E_\gamma < 9.5$ GeV (center), and $9.5 < E_\gamma < 10.6$ GeV (bottom). Clear indications of sub-threshold J/ψ production may be observed in helium and carbon.

Using the measured luminosity and simulated efficiency as a function of E_γ, as well correcting for nuclear transparency, we calculate the cross section for each nucleus, presently including only statistical and background-related uncertainties. In Fig. 14 we show the energy-dependent cross sections for helium and carbon. The data are compared with the plane-wave calculations for the cross section, split into mean-field and SRC contributions. Fig. 15 shows the yield-weighted combined cross section for helium and carbon compared to the plane-wave calculation. In each case, no substantial deviation from plane-wave predictions is observed, though a slight excess of sub-threshold events does seem to be present. Bin-centering for each energy bin was done by determining the value of E_γ at which the cross section equals the bin-averaged value, according to plane-wave calculations.

Fig. 16 shows the energy-averaged cross section for each nucleus for both the full energy range and the above-threshold region. Data are again compared with plane-wave predictions, and no substantial deviations are observed.

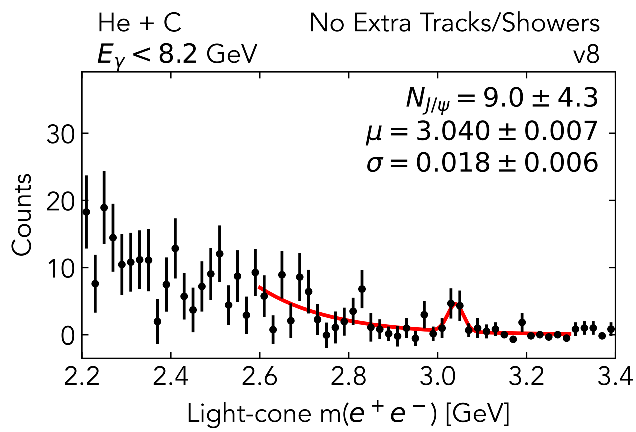

Figure 13: Dilepton invariant mass spectrum in the sub-threshold energy range $7 < E_\gamma < 8.2$ GeV, when combining data from helium and carbon targets. Combining the data of these nuclei allows a clear and statistically-significant observation of $J/\psi \to e^+e^-$ below threshold.

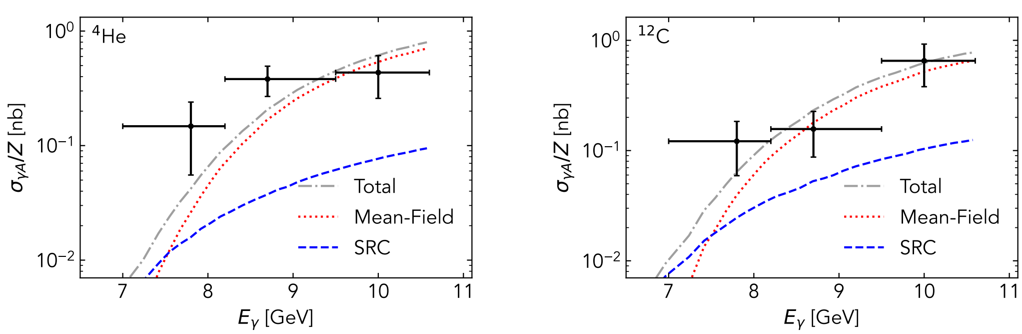

Figure 14: Measured cross sections for ^{4}He$(\gamma, J/\psi p)X$ (left) and ^{12}C$(\gamma, J/\psi p)X$ (right). In both cases the measured cross section (black) is compared with plane-wave calculations, including the Mean-Field (dotted red) and SRC (dashed blue) contributions as well as the total (dot-dashed grey).

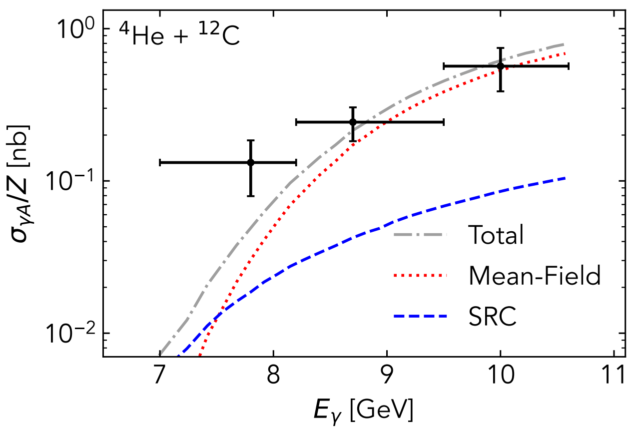

Figure 15: Luminosity-weighted average of the measured A($\gamma, J/\psi p$)X cross section for ^{4}He and ^{12}C, compared with plane-wave calculations for this average.

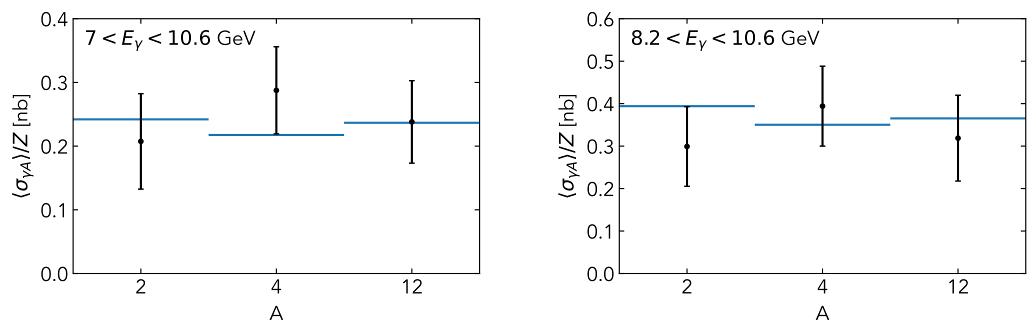

Figure 16: Measured cross sections for A($\gamma, J/\psi p$)X averaged over all photon energies $7 < E_\gamma < 10.8$ GeV (left) and above thoreshold $8.2 < E_\gamma < 10.8$ GeV (right). The measured data (black) are compared with the plane-wave predictions (blue).

References

[1] R. G. Arnold et al. "Measurements of the A Dependence of Deep-Inelastic Electron Scattering from Nuclei". In: *Phys. Rev. Lett.* 52 (9 Feb. 1984), pp. 727–730. DOI: 10.1103/PhysRevLett.52.727. URL: https://link.aps.org/doi/10.1103/PhysRevLett.52.727.

[2] J.J. Aubert et al. In: *Phys. Lett. B* 123 (1983), p. 275.

[3] J. Ashman et al. "Measurement of the ratios of deep inelastic muon-nucleus cross sections on various nuclei compared to deuterium". In: *Phys. Lett. B* 202 (1988), p. 603.

[4] J. Gomez et al. "Measurement of the A dependence of deep-inelastic electron scattering". In: *Phys. Rev. D* 49 (1994), p. 4348.

[5] M. Arneodo et al. "Measurements of the nucleon structure function in the range $0.002 < x < 0.17$ and $0.2 < Q^2 < 8$ GeV^2 in deuterium, carbon and calcium". In: *Nucl. Phys. B* 333 (1990), p. 1.

[6] J. Seely et al. "New Measurements of the European Muon Collaboration Effect in Very Light Nuclei". In: *Phys. Rev. Lett.* 103 (2009), p. 202301.

[7] B. Schmookler et al. "Modified structure of protons and neutrons in correlated pairs". In: *Nature* 566.7744 (2019), pp. 354–358. DOI: 10.1038/s41586-019-0925-9.

[8] Leonid Frankfurt and Mark Strikman. "Hard nuclear processes and microscopic nuclear structure". In: *Phys. Rep.* 160.5-6 (1988), pp. 235–427.

[9] M. M. Sargsian et al. "Hadrons in the nuclear medium". In: *J. Phys.* G29 (2003), R1.

[10] P R Norton. "The EMC effect". In: *Reports on Progress in Physics* 66.8 (July 2003), pp. 1253–1297. DOI: 10.1088/0034-4885/66/8/201. URL: https://doi.org/10.1088%2F0034-4885%2F66%2F8%2F201.

[11] O. Hen et al. "Nucleon-Nucleon Correlations, Short-lived Excitations, and the Quarks Within". In: *Rev. Mod. Phys.* 89.4 (2017), p. 045002. DOI: 10.1103/RevModPhys.89.045002.

[12] A. Ali et al. "First Measurement of Near-Threshold J/ψ Exclusive Photoproduction off the Proton". In: *Phys. Rev. Lett.* 123 (7 Aug. 2019), p. 072001. DOI: 10.1103/PhysRevLett.123.072001. URL: https://link.aps.org/doi/10.1103/PhysRevLett.123.072001.

[13] B. Duran et al. "Determining the gluonic gravitational form factors of the proton". In: *Nature* 615.7954 (2023), pp. 813–816.

[14] S. Adhikari et al. "Measurement of the J/ψ photoproduction cross section over the full near-threshold kinematic region". In: *Phys. Rev. C* 108 (2 Aug. 2023), p. 025201. DOI: 10.1103/PhysRevC.108.025201. URL: https://link.aps.org/doi/10.1103/PhysRevC.108.025201.

[15] Paul Hoyer. "Physics at ELFE". In: *Nuclear Physics A* 622.1 (1997), pp. c284–c314.

[16] Paul Hoyer. *Charmonium Production at ELFE Energies.* 1997. arXiv: hep-ph/9702385 [hep-ph].

[17] P. Bosted et al. "Search for sub-threshold photoproduction of J/ψ mesons". In: *Phys. Rev. C* 79 (1 Jan. 2009), p. 015209. DOI: 10.1103/PhysRevC.79.015209. URL: https://link.aps.org/doi/10.1103/PhysRevC.79.015209.

[18] Yoshitaka Hatta et al. "Sub-threshold J/ψ and Υ production in *gamma*A collisions". In: *Physics Letters B* 803 (Apr. 2020), p. 135321. DOI: 10.1016/j.physletb.2020.135321. URL: https://doi.org/10.1016%2Fj.physletb.2020.135321.

[19] S.J. Brodsky et al. "Photoproduction of charm near threshold". In: *Physics Letters B* 498.1-2 (Jan. 2001), pp. 23–28. DOI: 10.1016/s0370-2693(00)01373-3. URL: https://doi.org/10.1016%2Fs0370-2693%2800%2901373-3.

[20] B. Gittelman et al. "Photoproduction of the $\psi(3100)$ Meson at 11 GeV". In: *Phys. Rev. Lett.* 35 (24 Dec. 1975), pp. 1616–1619. DOI: 10.1103/PhysRevLett.35.1616. URL: https://link.aps.org/doi/10.1103/PhysRevLett.35.1616.

[21] U. Camerini et al. "Photoproduction of the ψ Particles". In: *Phys. Rev. Lett.* 35 (8 Aug. 1975), pp. 483–486. DOI: 10.1103/PhysRevLett.35.483. URL: https://link.aps.org/doi/10.1103/PhysRevLett.35.483.

[22] *DSelector*. 2022. URL: https://halldweb1.jlab.org/wiki/index.php/DSelector.

[23] A. Ali et al. "First Measurement of Near-Threshold J/ψ Exclusive Photoproduction off the Proton". In: *Physical Review Letters* 123.7 (Aug. 2019). DOI: 10.1103/physrevlett.123.072001. URL: https://doi.org/10.1103%2Fphysrevlett.123.072001.

[24] S. Adhikari et al. *Measurement of the J/ψ photoproduction cross section over the full near-threshold kinematic region.* 2023. arXiv: 2304.03845 [nucl-ex].

[25] E. Piasetzky et al. "Evidence for the strong dominance of proton-neutron correlations in nuclei". In: *Phys. Rev. Lett.* 97 (2006), p. 162504. DOI: 10.1103/PhysRevLett.97.162504. arXiv: nucl-th/0604012 [nucl-th].

[26] Ji Xu and Feng Yuan. "Gluonic probe for the short range correlation in nucleus". In: *Physics Letters B* 801 (Feb. 2020), p. 135187. DOI: 10.1016/j.physletb.2019.135187. URL: https://doi.org/10.1016%2Fj.physletb.2019.135187.

[27] N. Rocco and A. Lovato. private communication.

[28] Ronen Weiss et al. "Energy and momentum dependence of nuclear short-range correlations - Spectral function, exclusive scattering experiments and the contact formalism". In: *Phys. Lett.* B791 (2019), pp. 242–248. DOI: 10.1016/j.physletb.2019.02.019. arXiv: 1806.10217 [nucl-th].

[29] A. Schmidt et al. "Probing the core of the strong nuclear interaction". In: *Nature* 578.7796 (2020), pp. 540–544. DOI: 10.1038/s41586-020-2021-6. arXiv: 2004.11221 [nucl-ex].

[30] J.R. Pybus et al. "Generalized contact formalism analysis of the ^{4}He$(e, e'pN)$ reaction". In: *Phys. Lett. B* 805 (2020), p. 135429. DOI: 10.1016/j.physletb.2020.135429. arXiv: 2003.02318 [nucl-th].

[31] S. Veerasamy and W. N. Polyzou. “Momentum-space Argonne V18 interaction”. In: *Phys. Rev. C* 84 (3 2011), p. 034003.

[32] R. B. Wiringa et al. “Nucleon and nucleon-pair momentum distributions in $A \leq 12$”. In: *Phys. Rev. C* 89 (2 Feb. 2014), p. 024305.

[33] S. Adhikari et al. “The GlueX beamline and detector”. In: *Nuclear Instruments and Methods in Physics Research Section A: Accelerators, Spectrometers, Detectors and Associated Equipment* 987 (2021), p. 164807. ISSN: 0168-9002. DOI: https://doi.org/10.1016/j.nima.2020.164807. URL: https://www.sciencedirect.com/science/article/pii/S0168900220312043.

[34] D. Abbott et al. “Quasifree \(e,e’p\) Reactions and Proton Propagation in Nuclei”. In: *Phys. Rev. Lett.* 80.23 (June 1998), pp. 5072–5076. DOI: 10.1103/PhysRevLett.80.5072.

[35] K Garrow and et. al. “Nuclear transparency from quasielastic A(e,e’p) reactions up to Qsup 2=8.1 (GeV/c)sup 2”. In: *Physical Review C* 66.04 (Aug. 2001). DOI: 10.1103/PhysRevC.66.044613. URL: https://www.osti.gov/biblio/785455.

A Flux

One of the important tasks of the Hall D pair spectrometer (PS) is to determine a flux of collimated beam photons incident on the GlueX target, which is needed to measure cross sections of various physics processes. The photon flux is obtained by reconstructing electron-positron pairs produced by beam photons during the physics run. The PS was integrated into the GlueX trigger system and allowed to record e^+e^- candidates in parallel with taking experimental data. The number of beam photons (N_γ) is related to the number of electron-positron pairs, ($N_{e^+e^-}$), detected by the pair spectrometer according to the following expression:

$$N_\gamma = \frac{N_{e^+e^-}}{N_{\rm conv}\,\sigma_{e^+e^-}\,\epsilon\,A}, \qquad (13)$$

where $N_{\rm conv}$ is the number of atoms in the pair spectrometer converter, $\sigma_{e^+e^-}$ is the pair production cross section, ϵ is the efficiency of detecting leptons in the PS counters, and A is the PS acceptance. The denominator in Eq. 13, $K = N_{\rm conv}\,\sigma_{e^+e^-}\,\epsilon\,A$, was obtained during PS calibration runs, where we simultaneously measured the number of electromagnetic pairs and the number of photons in the beam . For the calibration, we used a small electromagnetic calorimeter, which was inserted into the photon beam and allowed us to directly count the number of beam photons.

The tagged photon energy distribution is used in the event generator by randomly selecting a beam photon energy according to this distribution. The tagged energy spectra are determined from the PS data for every run in the SRC experiment and are stored in the calibration database. The Hall D simulation framework allows to generate MC samples according to realistic run-by-run dependent distributions of tagged photon energy spectra and electron beam energies.

A.1 Non-target hits for flux ratio determination

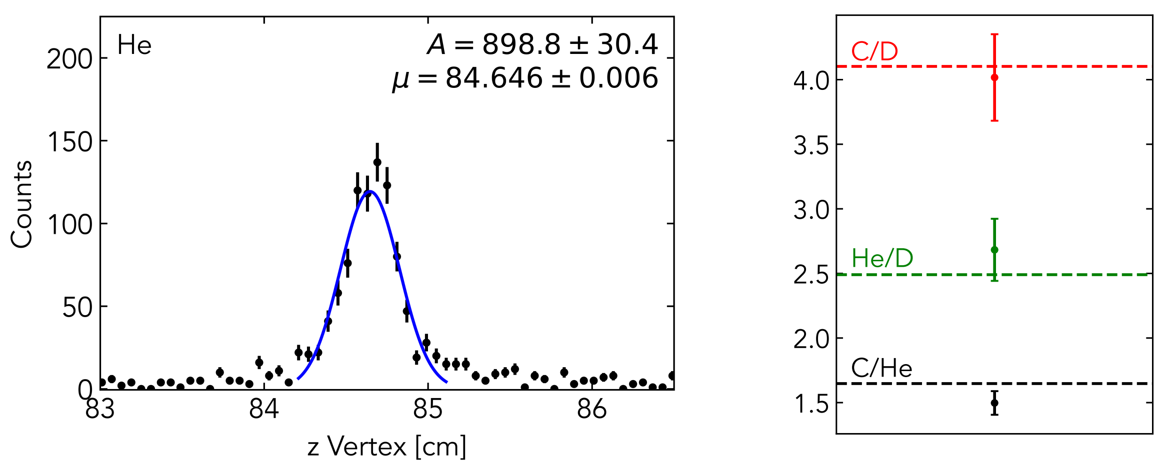

Figure 17: *Left:* Gaussian fit of non-target vertex peak centered near 84.6, behind the target. *Right:* Ratio of gaussian peak heights (error bars) compared to measured flux valuse (dashed lines) between all three targets.

B Extended Figures

B.1 p/E Fitting

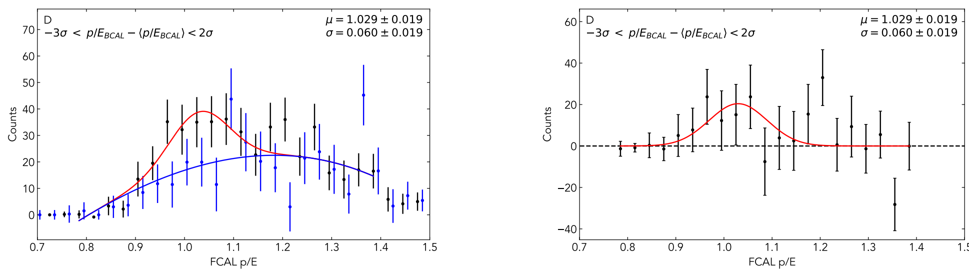

Figure 18: *Left:* Distributions of p/E for FCAL lepton candidates, including the signal slice (black) and the background slice (blue) normalized to the same background contribution. The background polynomial fit (blue line) and as well as the Gaussian signal (red line) are shown with the data. *Left:* Difference between signal and background slices, normalized to the fit coefficient for the polynomial background contribution. The Gaussian description of the lepton signal is also shown.

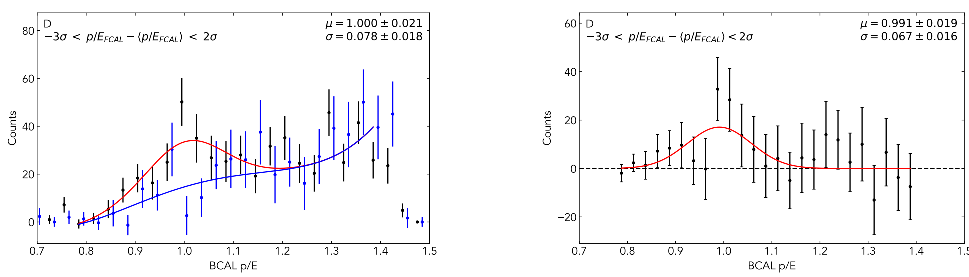

Figure 19: Same as Fig. 6 but for BCAL lepton candidates.

B.2 Light-cone Mass Comparison

B.3 Kinematic Distributions

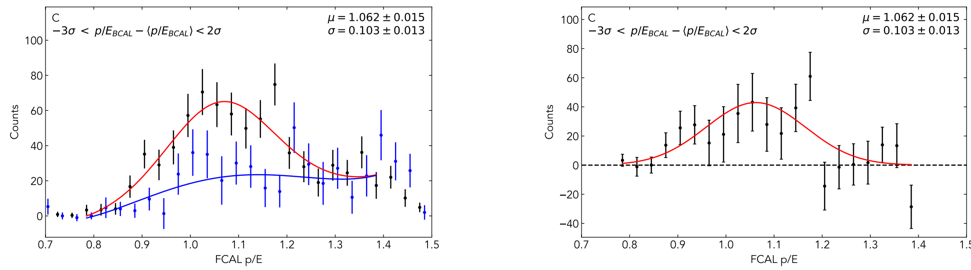

Figure 20: *Left:* Distributions of p/E for FCAL lepton candidates, including the signal slice (black) and the background slice (blue) normalized to the same background contribution. The background polynomial fit (blue line) and as well as the Gaussian signal (red line) are shown with the data. *Left:* Difference between signal and background slices, normalized to the fit coefficient for the polynomial background contribution. The Gaussian description of the lepton signal is also shown.

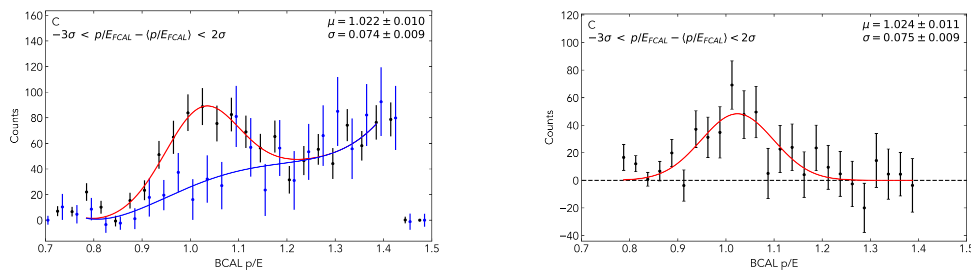

Figure 21: Same as Fig. 6 but for BCAL lepton candidates.

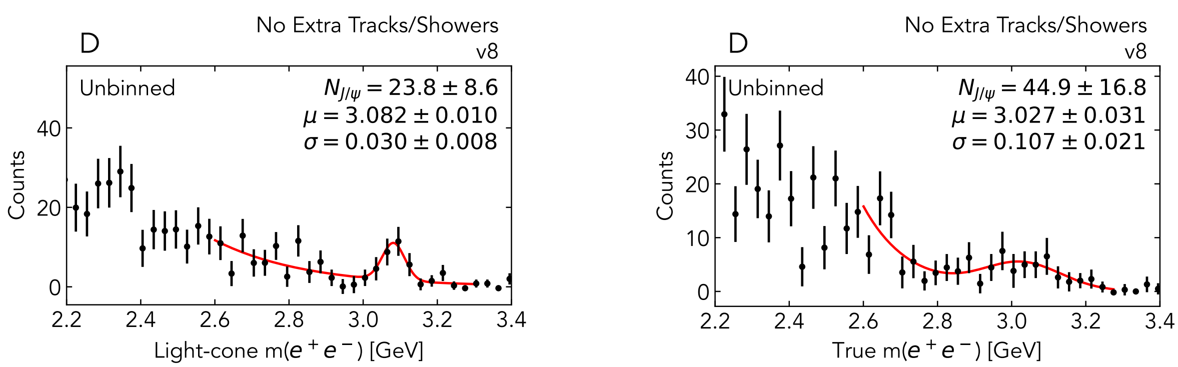

Figure 22: Di-lepton pair invariant mass. Left: Light-cone proxy variable. Right: True invariant mass.

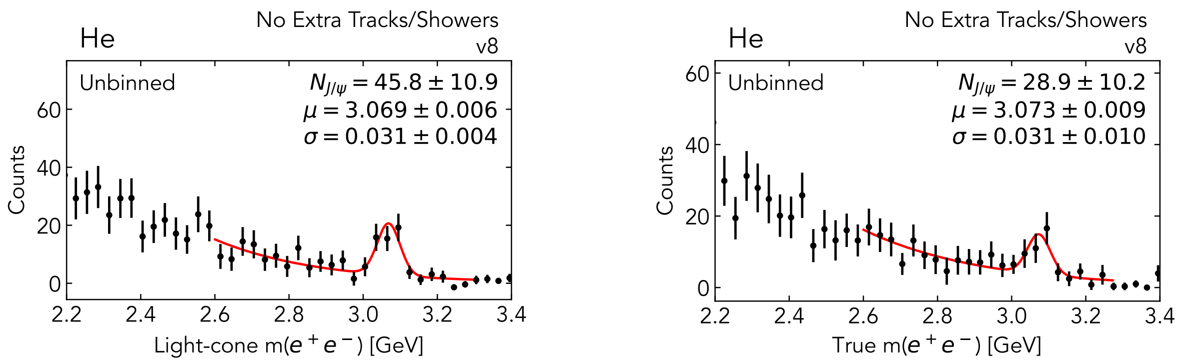

Figure 23: Di-lepton pair invariant mass. Left: Light-cone proxy variable. Right: True invariant mass.

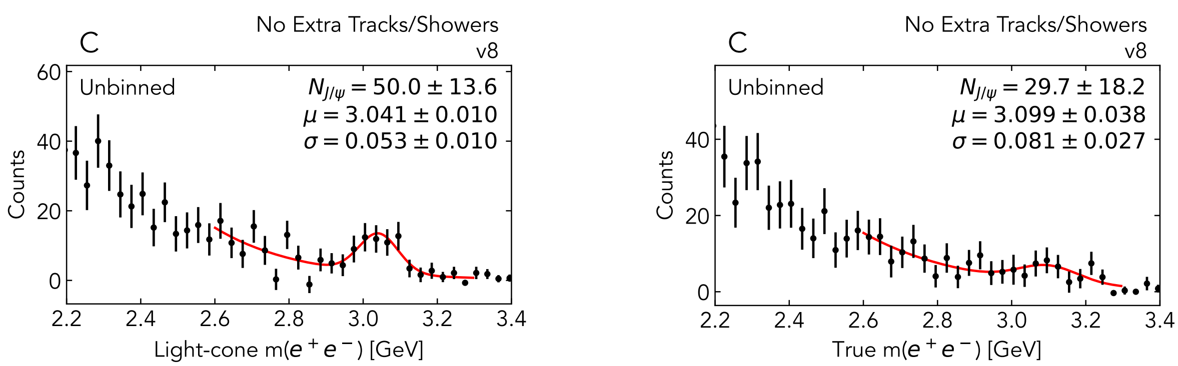

Figure 24: Di-lepton pair invariant mass. Left: Light-cone proxy variable. Right: True invariant mass.

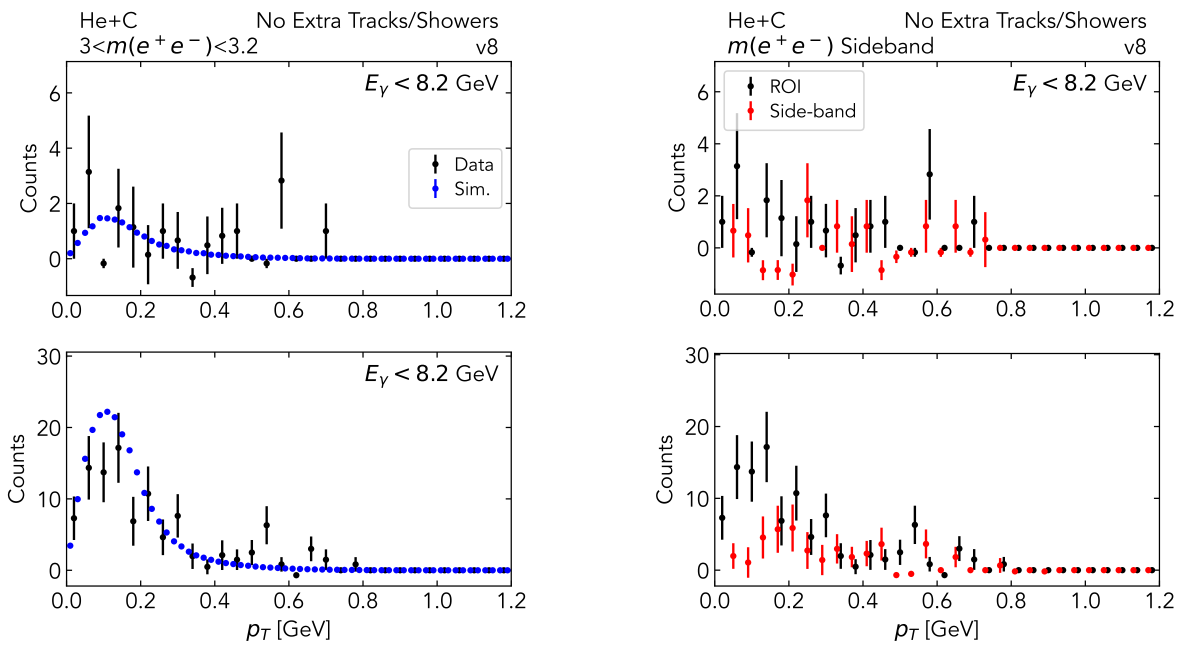

Figure 25: p_T

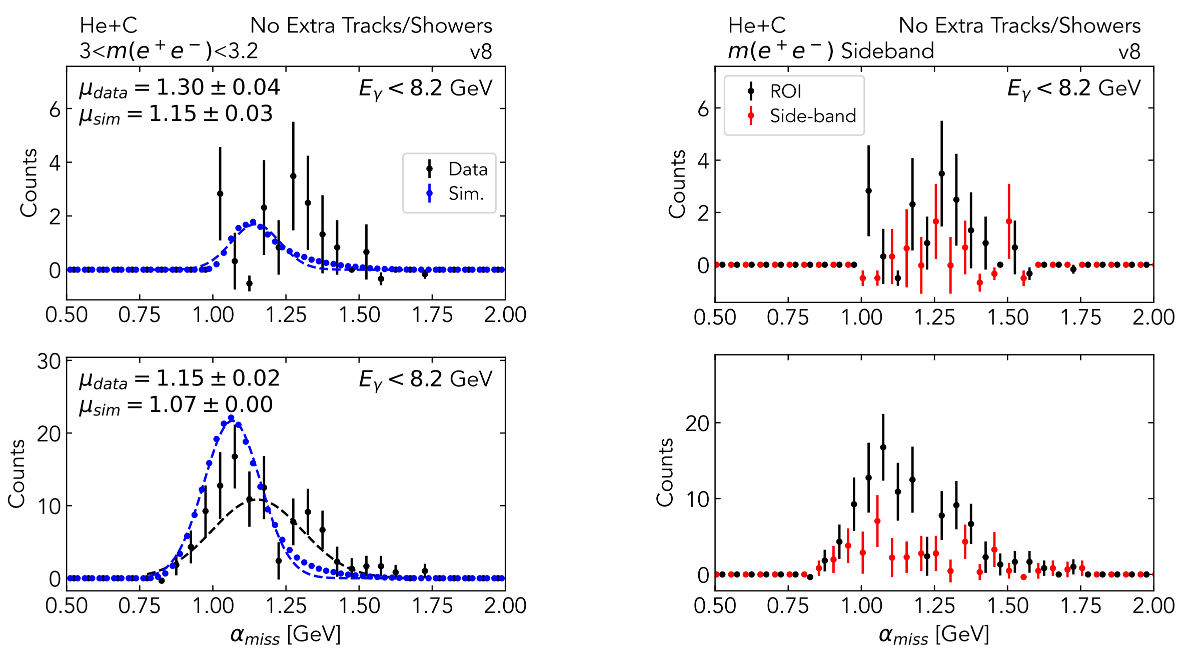

Figure 26: α_{miss}

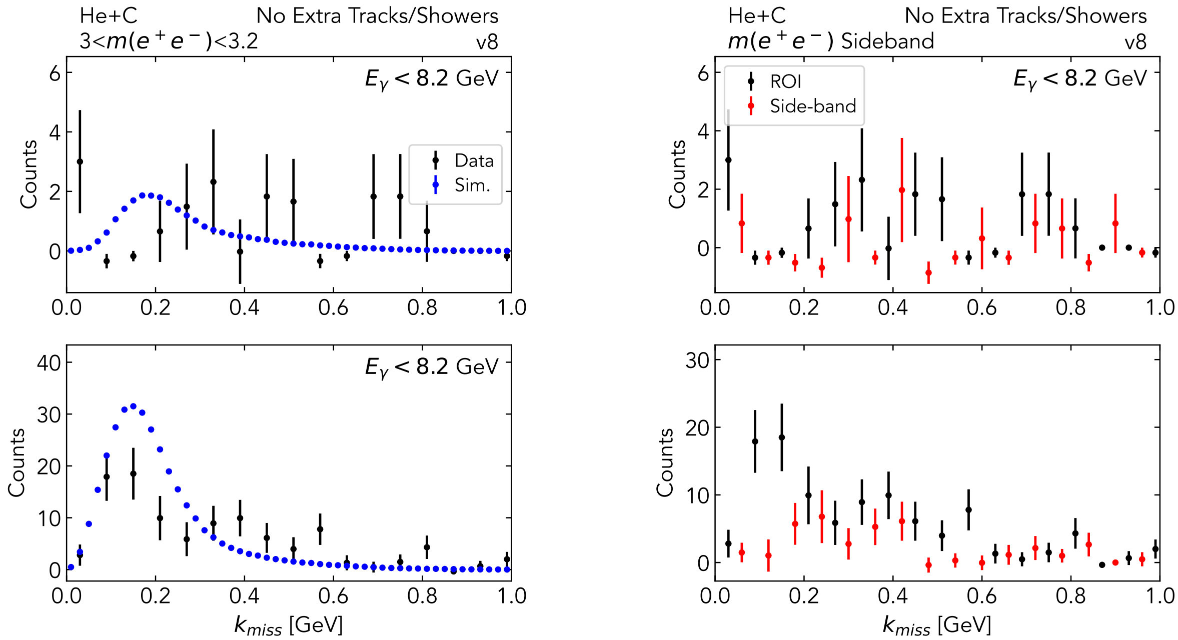

Figure 27: K_{miss}

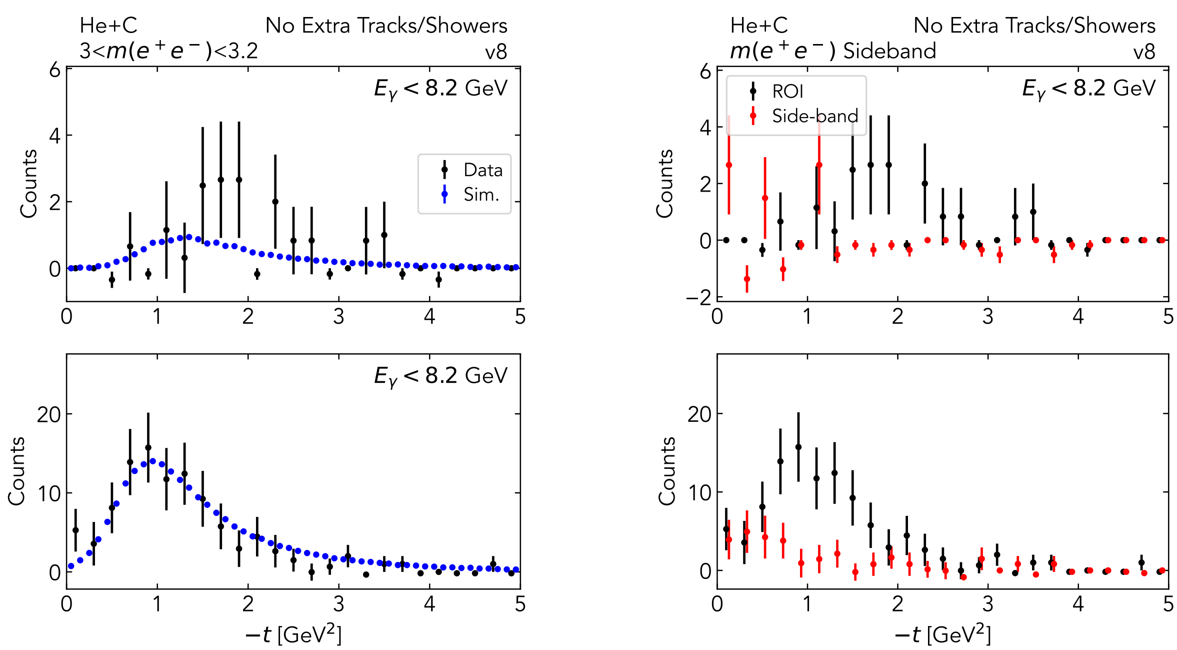

Figure 28: t